Available at www.sciencedirect.com

ScienceDirect

journal homepage: www.elsevier.com/locate/he

Experimental and numerical studies of local current mapping on a PEM fuel cell

J.J. Hwnag[a], W.R. Chang[b,*], R.G. Peng[c], P.Y. Chen[d], A. Su[e]

[a]Department of Environment and Energy, National University of Tainan, Tainan 700, Taiwan
[b]Department of Landscape Architecture, Chung-Hua University, Hsinchu 300, Taiwan
[c]Department of Mechanical Engineering, National Chiao Tong University, Hsinchu 300, Taiwan
[d]Department of Power Mechanical Engineering, National Tsing Hua University, Hsinchu 300, Taiwan
[e]Department of Mechanical Engineering and Fuel Cell Center, Yuan Ze University, Taoyuan, Taiwan

ARTICLE INFO

Article history:
Received 16 April 2008
Received in revised form
6 July 2008
Accepted 8 July 2008
Available online 14 September 2008

Keywords:
PEM fuel cell
MEA
Hall-effect sensor
Current

ABSTRACT

Local current distribution on a PEM fuel cell has been mapped experimentally by using a special-designed single cell fixture. It is composed of a composite cathodic flow-field plate, a membrane electrode assembly (MEA) and a stainless-steel anodic flow-field plate. An array of 16 individual conductive segments was distributed on the composite plate. A self-made MEA is in direct contact with the segmented current collectors. Regional-averaged current through each segment is determined by using the Hall-effect sensor. To ensure the data reliability, a comparison of polarization curves was made between the composite flow-field plate and the conventional flow-field plate. Then, the effects of flow-field patterns, dew points of the cathodic feedings and cathodic stoichiometrics on the local current distribution were examined. The transient variation of the local current distribution on the cathode under supersaturated conditions was further visualized to illustrate the flooding phenomena in different flow patterns. This technique developed by the present work has contributed to knowledge and understanding the local current distributions in a PEM fuel cell that is helpful in designing the fuel-cell components.

1. Introduction

Owing to many advantages accompanied by proton exchange membrane (PEM) fuel cells, such as non-pollution, high efficiency, low noise and quick startup, they have been regarded as the most potential power system for the ultimate eco-vehicles. In the past decade, almost all major car manufacturers in the world have devoted themselves to the development of PEM fuel cell vehicles. However, there still have been some challenges about PEM fuel-cell technologies that need to be overcome, especially in prolonging the lifetime of the PEM fuel cell [1].

It is well known that the lifetime of a PEM fuel cell depends strongly on the local current distribution on the electrode. Uneven distribution of local current on the electrode means irregularity of the electrochemical reaction on the reacting site. It not only reduces the cell performance but also shortens its lifetime. The local current distribution on a PEM fuel cell will be affected by many factors, such as cell temperature, degree of humidification, partial pressure of the feeding gases, configuration of the flow channels, microstructures and characteristics of the electrodes [2–4], etc. Therefore, it is very important to understand the above effects on local current distribution for designing and operating a PEM fuel cell.

* *Corresponding author*. Tel.: +886 3374281.
E-mail address: ruby@chu.edu.tw (W.R. Chang).
0360-3199/$ – see front matter © 2008 International Association for Hydrogen Energy. Published by Elsevier Ltd. All rights reserved.
doi:10.1016/j.ijhydene.2008.07.035

Nomenclature

c_{O_2}	concentration of oxygen (mol m^{-3})
c_{H_2O}	concentration of water vapor (mol m^{-3})
D_{H_2O}	diffusivity of water vapor (m^2 s^{-1})
$D_{H_2O,eff}$	effective diffusivity of water vapor (m^2 s^{-1})
D_{O_2}	diffusivity of oxygen (m^2 s^{-1})
$D_{O_2,eff}$	effective diffusivity of oxygen (m^2 s^{-1})
F	faradays constant (96 487 C mol^{-1})
i	local current density (A m^{-2})
i_o	exchange current density (A m^{-2})
i_{ct}	local transfer current density
p	pressure (Pa)
R	universal gas constant (W mol^{-1} K^{-1})
T	temperature (K)
M	molecular weight (kg mol^{-1})
S_a	surface area-to-volume ratio of the porous matrix (m^{-1})
U	operational voltage of the single cell (V)
u	velocity vector (m s^{-1})
x, y, z	coordinates system (m)

Greek symbols

ξ	reactant stoichiometry
κ	permeability (m^2)
ϵ	cathode porosity
ρ	density (kg m^{-3})
η	overpotential (V)
τ	tortuosity
α	symmetric factor
μ	dynamic viscosity (m s^{-2})
φ	potential (V)
ω	mass fraction

Suffix

a	anode
c	cathode
cell	cell
dp	dew point
eff	effective
in	inlet
out	outlet
ref	reference

In the past, many experimental researches have published concerning the local current distribution in a PEM fuel cell [5–19]. Some works rely on the numerical simulation [20–28]. However, studies reported that both experimental and numerical results are rather sparse, which motivates the present work to map the local current on the PEM fuel cell numerically and experimentally. Experimental evidence not only confirms the numerically calculated results but also gives a better understanding of the nature of the electrochemical reactions occurring inside the cell. Thus, the local current distribution by direct measurement can offer essential references for designs of cells, stacks and even systems of the PEM fuel cell. In the present work, a special-designed fixture is used to in-situ map the local current distribution on the electrode of a PEM fuel cell. An array of 4 by 4 segmental current collectors is distributed on the cathodic flow-field plate. Each conductive segment is insulated mutually. Current through each current collector is measured individually by using a Hall-effect sensor, which well represents the regionally averaged data on its counterpart. A self-made MEA is integrated into the above single-cell fixture for local current measurement. Parametric studies include the cathodic flow-field patterns (parallel, serpentine, interdigitated and biomimic flow fields), the cathodic-feeding stoichiometries ($\xi_c = 2.5$–3.5) and the dew point of cathodic feedings ($T_{dp,c} = 40$–$70\,^\circ$C). First, the experiments are compared with the numerical simulation results to verify the reliability of the instruments. In addition, to ensure the data consensus, a comparison of polarization curves is made between the composite flow-field plate and the conventional flow-field plate. Moreover, the evolution of local current distribution on the cathode of the parallel and serpentine flow fields under supersaturated conditions are visualized and compared thereafter. It can give an evidence to explain the reason why the parallel flow field is easier flooded in the electrode than the serpentine flow field. Finally, the influences of flow-field pattern and stoichiometry variation of feeding gases are discussed in terms of the measured local current distribution in the segmented single cell.

2. Experiment

Fig. 1 (a) shows a photo of the special-designed single-cell fixture for local current measurements, while Fig. 1 (b) is the corresponding assembly diagram. The fixture consists of a cathodic flow-field plate, an anodic flow-field plate, an MEA and other assisting parts (such as fittings, screws, gaskets, etc.). The anodic flow-field plate is made of stainless steel, while the cathodic counterpart is a composite plate that is made of a polyoxymethylene (POM) frame infixed a number of stainless-steel current collectors. As shown in Fig. 2, on the composite plate, the active surface is divided by 4 by 4 segments. Sixteen pieces of stainless-steel blocks of dimension 9 mm × 9 mm × 12 mm are inserted into a pre-machined POM frame with a space of 2.5 mm in between. They are electrically insulated from each other. All stainless-steel blocks are coated with a thin layer of titanium on surface of to prevent the possible corrosion. In addition, to ensure leakage free of the composite plate, the epoxy resin is used to fill gaps between the POM frame and the stainless steel blocks. After the epoxy is dried, the flow-field channels are carved on the surface of the composite plate using the CNC machine. As shown in Fig. 3, four kinds of flow fields are tested in the present work, i.e., a parallel flow field, a serpentine flow field, an interdigitated flow field, and a biomimic flow field, respectively. The depth of flow channels is 1.0 mm and the reactive surface is 5.0 cm × 5.0 cm. Note that the open-area ratios of the above four flow fields ranged from 53% to 58%. Under the same clamping pressure, the Ohmic resistance for current passing through interface between the gas diffusion layers and the flow-field plate can be regarded as the same [13]. As for the anodic plate, the surface is machined with a serpentine flow field that is the same as the cathodic

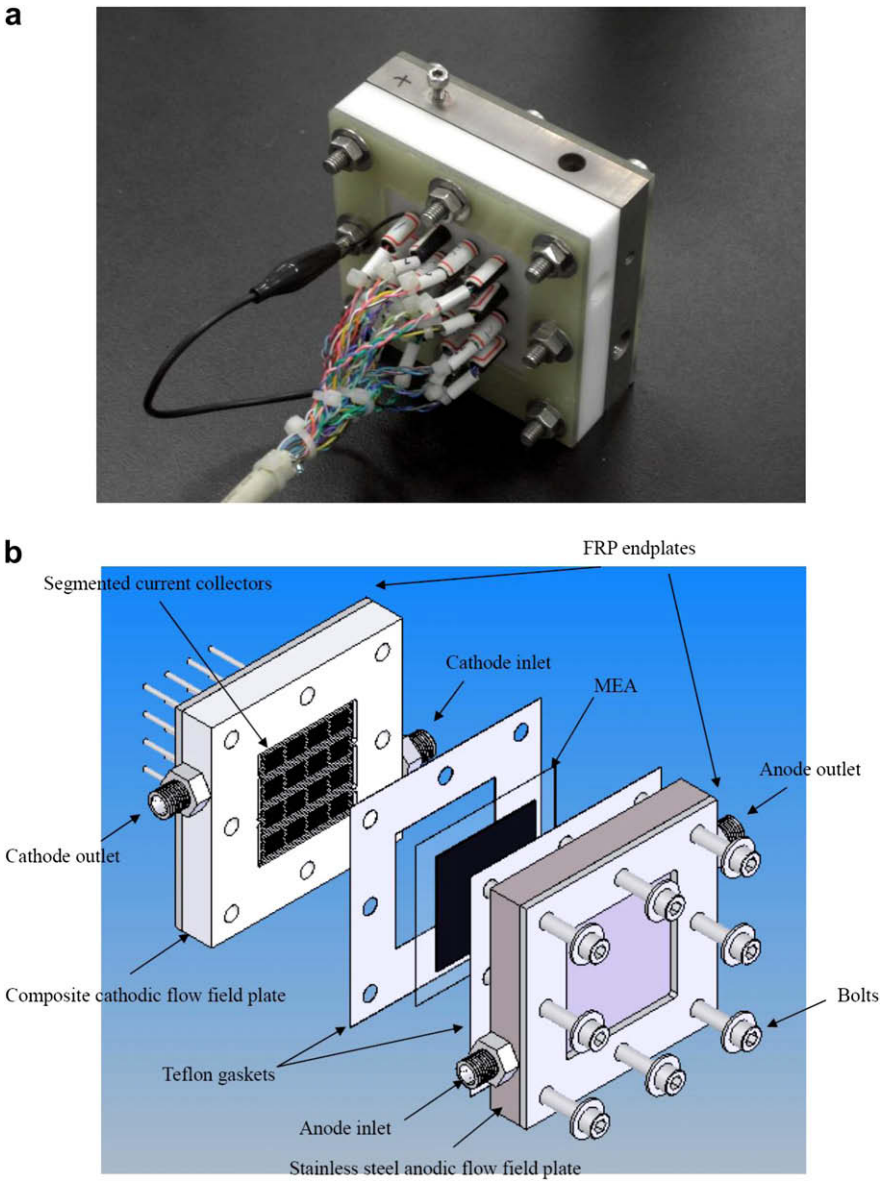

Fig. 1 – Test fixture of local current measurement, (a) photo of the test fixture and (b) assembly diagram of the test fixture.

counterpart. Its surface is also coated with a thin layer of titanium to prevent the possible erosion. Note that the anode keeps its flow pattern when the effect of the flow-field on the cathodic plate is examined.

The MEA used in the present work is prepared as the following processes [14]. First, the membranes Nafion® 112 are soaked in a mixture of H_2O_2/H_2O at approximately 80 °C for 2 h, and then are washed with distilled water to remove the organic and mineral impurities. Subsequently, the transparent Nafion® membranes are soaked in a 1 M boiling H_2SO_4 solution for 2 h. Finally, they are rinsed again to remove excess H_2SO_4, and thus the membranes, being ready to use, are stored in distilled water. Subsequently, the commercially available electrocatalyst, 20% platinum on Vulcan XC-72 carbon (from E-Tek), is suspended in an aqueous Nafion® solution, which is then well mixed by using an ultrasonic bath. The above mixture is then printed directly onto two sides of the membrane as active layers, rather than deposed onto gas diffusion layers (carbon papers). The amounts of Pt and Nafion® on the electrode were about 0.2 and 0.6 mg/cm^2, respectively. As for the gas diffusion layers, composed 20% Pt/C and 0.2 Pt mg/cm^2, for both electrodes is added to the carbon papers. The five-layer MEA is assembled conventionally, using a hot pressing process conducted at 140 °C and 8.0 Mpa for 90 s. The active surface area of the MEA is 25 cm^2.

As shown in Fig. 4, the current on each segment is conducted to a multiplexer consisted of 16 Hall-effect sensors. The assembled single-cell fixture is then installed on a commercial test stand (APFCT FCED 200) that controls all operational conditions such as dew points of feeding gases, cell temperature and backpressure. Table 1 lists the MEA configurations and details of the operation conditions.

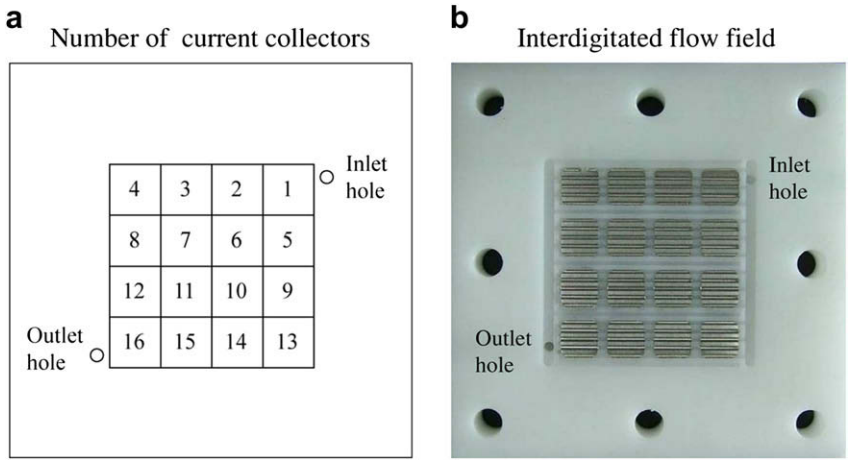

Fig. 2 – Locations of the current collectors and their corresponding number on the composite flow-field plate.

3. Numerical model and scheme

To realize the electrochemical reactions within the flow field of the fuel cell, a numerical approach is conducted to compare with the experiment data. The details of the model have been discussed elsewhere and only some important features are described here.

The oxygen reduction reaction (ORR) takes place on the three-phase boundary (TPB) of the porous cathode. It can be represented by the following equations.

$$O_2 + 4H^+ + 4e^- \rightarrow 2H_2O \quad (1)$$

Note that the breathing holes are not only the entrance of the fresh air but also the exit of the products (water vapor) of the electrochemical reaction.

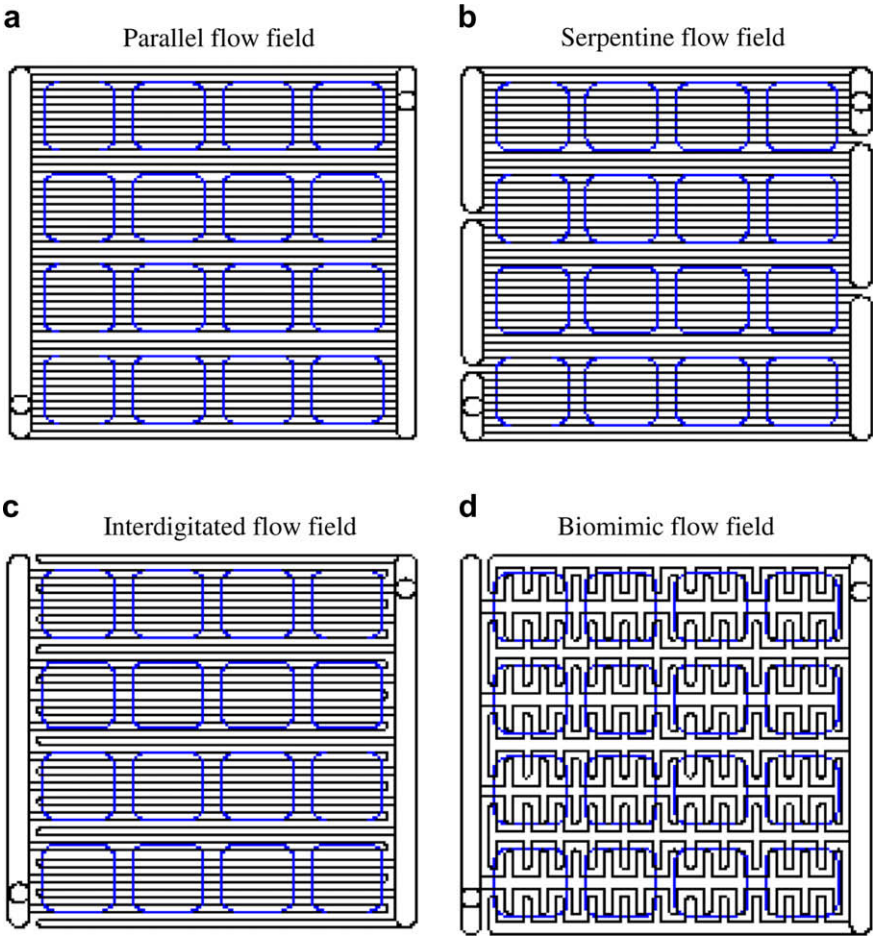

Fig. 3 – Investigated flow patterns on the cathodic flow-field plates.

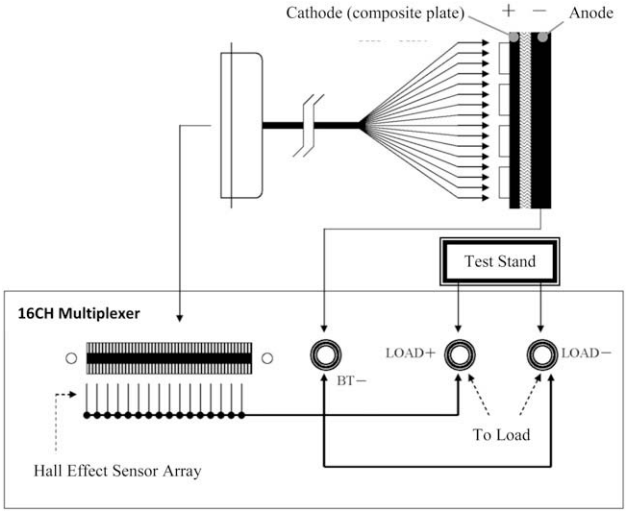

Fig. 4 – Configuration of the 16-channel multiplexer for local current measurements.

The momentum and mass conservations for the gas flow mixture in the porous cathode are described as follows:

$$\frac{1}{\epsilon}\nabla\cdot(\rho\mathbf{u}\mathbf{u}) = -\varepsilon\nabla p + \nabla\cdot(\mu\nabla\mathbf{u}) + \frac{\varepsilon\mu\mathbf{u}}{\kappa} \tag{2}$$

$$\nabla(\rho\mathbf{u}) = \frac{i_{ct}S_a M}{4F} \tag{3}$$

where ρ is the density of the gas mixture; $\mathbf{u}$, the velocity vector; κ, the permeability; ε, the porosity; μ, the viscosity and p is the pressure. As for the mass conservation, the electrochemical reaction occurring on the TPB acts as a sink of oxygen and, simultaneously, a source of water vapor. S_a is the surface area-to-volume ratio of the porous matrix; i_{ct}, the local transfer current density; M, the mole masses of gas mixtures and F is the Faraday's constant.

The species conservations for oxygen, water vapor and nitrogen in the multi-component system are expressed respectively as

Table 1 – .Parametric conditions of the experiment

Cell	PEM	Nafion® 112
	Reaction area	25 cm^2
	Pt loading	0.2 mg/cm^2 for anode and cathode
	GDL	E-Tech for anode and cathode
	Cell temperature, T_{cell}	40, 50, 60 °C
Anode feeding	H_2	Pure (>99.99%)
	Dew point, $T_{dp,a}$	40 °C
	Stoichiometry (flow rate), ξ_a	1.5
Cathode feeding	O_2	Pure
	Dew point, $T_{celldp,c}$	40, 50, 60, 70 °C
	Stoichiometry (flow rate), ξ_c	2.5, 3.0, 3.5

$$\nabla\cdot(\rho\mathbf{u}\omega_{O_2}) = \rho D_{O_2,\mathrm{eff}}\nabla^2\omega_{O_2} + \frac{\rho\omega_{O_2}}{M}D_{O_2,\mathrm{eff}}\nabla M - \sum_j D_{j,\mathrm{eff}}\nabla(M\omega_j) + S_{O_2} \tag{4}$$

$$\nabla\cdot(\rho\mathbf{u}\omega_{H_2O}) = \rho D_{H_2O,\mathrm{eff}}\nabla^2\omega_{H_2O} + \frac{\rho\omega_{H_2O}}{M}D_{H_2O,\mathrm{eff}}\nabla M - \sum_j D_{j,\mathrm{eff}}\nabla(M\omega_j) + S_{H_2O} \tag{5}$$

$$\omega_{N_2} = 1 - \omega_{O_2} - \omega_{H_2O} \tag{6}$$

In Eqs. (4) and (5), the first term on the right-hand side represents the Fickian diffusion, while the second and third terms are the modification to enforce the Stefan–Maxwell equations on the multi-component diffusive system. The source terms for the mass balances for oxygen and water vapor are given, respectively, by

$$S_{O_2} = -\frac{i_{ct}S_a M_{O_2}}{4F} \tag{7}$$

$$S_{H_2O} = \frac{i_{ct}S_a M_{H_2O}}{2F} \tag{8}$$

As for the effective diffusivities of the oxygen $(D_{O_2,\mathrm{eff}})$ and water vapor $(D_{H_2O,\mathrm{eff}})$ in the porous cathode, they follow the Bruggemann model, i.e.,

$$D_{O_2,\mathrm{eff}} = \varepsilon^{\tau}D_{O_2} \tag{9}$$

$$D_{H_2O,\mathrm{eff}} = \varepsilon^{\tau}D_{H_2O} \tag{10}$$

The local transfer current density i_{ct} *in Eqs. (3), (7) and (8) is depicted by the Butler–Volmer correlation [12].*

$$i_{ct} = i_o\left\{\left(\frac{c_{O_2}}{c_{O_2,\mathrm{ref}}}\right)\exp\left[\frac{4\alpha F}{RT}(\phi_l - \phi_s)\right] - \left(\frac{c_{H_2O}}{c_{H_2O,\mathrm{ref}}}\right)^2\exp\left[\frac{4(1-\alpha)F}{RT}(\phi_l - \phi_s)\right]\right\} \tag{11}$$

where α is the symmetric factor and T *is the temperature. c_{O_2} and c_{H_2O} are the concentrations of oxygen and water vapor, respectively.* $\varphi_l - \varphi_s$ is the potential difference between the electrolyte phase and the catalyst phase in the porous electrode. It drives the transfer current density from the electrolyte phase to the catalyst phase that keeps the electrochemical reaction continuously.

The above governing equations are numerically solved by using a commercial code [29,30]. Computations are performed on 2252 unstructured meshes. Additional runs for the coarser meshes, 1832, and the finer meshes, 2682, are taken for a check of grid independence. The program gives results within 1% of each other on the finest meshes used. A typical simulation requires about 300 min of central processing unit time on a Pentium IV 2.8 GHz PC.

4. Results and discussions

4.1. *Validation of the measurement technique*

Before the discussion of the experimental results, it is necessary to validate the present instruments for local current

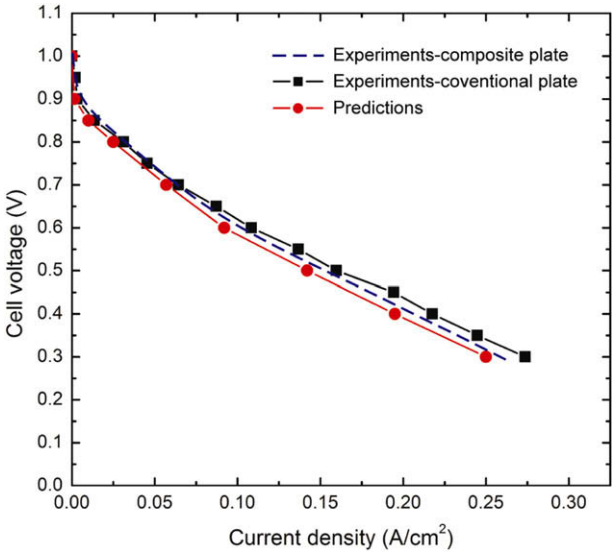

Fig. 5 – Comparison of the polarization curves between the present composite cathodic flow-field plate and the conventional flow-field plate, $T_{cell} = 40\,^{\circ}C$, $\xi_a = 1.5$ and $\xi_c = 2.5$.

measurements. Fig. 5 compares the polarization curves between the composite single cell (dashed line) and the conventional single cell (square symbol). The cell operational temperature is fixed $T_{cell} = 40\,^{\circ}C$. The stoichiometries for the anodic and cathodic feeding are fixed at $\xi_a = 1.5$ and $\xi_c = 2.5$, respectively. It is seen that these two polarization curves almost fall into a single curve. The consensus of data between these two techniques means the present instruments are reliable. Fig. 6 further confirms the present technique by comparing the local current distributions between the numerical predictions and the experimental measurements at the cell voltage of $U = 0.5$ V. Qualitatively, the local current distributions are largely similar between measured and predicted results. Both results reveal a local maximum near the entrance of the flow-field plate, and a local minimum near the outlet of the flow-field plate. In quantity, the predicted and measured averaged current densities are 142 and 158 mA/cm^2, respectively, with an error about 10%. Generally, the agreement between the above results is satisfactory.

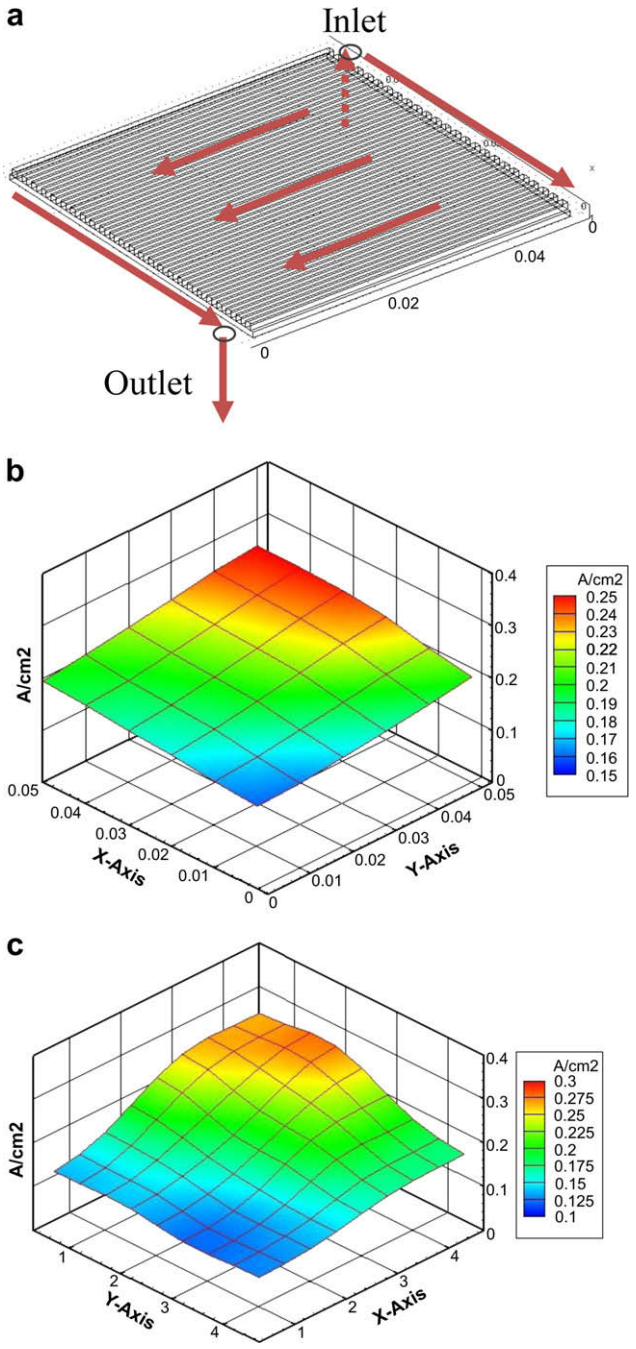

Fig. 6 – Comparison of the numerical predictions and the experimental measurement, (a) flow direction, (b) numerical results and (c) experimental results, $U = 0.5$ V, $T_{cell} = 40\,^{\circ}C$, $\xi_a = 1.5$ and $\xi_c = 2.5$.

4.2. *Evolution of current distribution*

Fig. 7 shows a comparison of transient developments of local current distributions on two different flow-field plates under supersaturated conditions, i.e., the parallel flow-field plate and the serpentine flow-field plate. It can provide a comparative assessment of the capability of water management between these two flow fields. The cell voltage is fixed at $U = 0.5$ V, while the stoichiometries of anodic and cathodic feedings are $\xi_a = 1.5$ and $\xi_c = 2.5$, respectively. The cell operational temperature is fixed at $T_{cell} = 40\,^{\circ}C$. The anodic feeding is saturated with a dew point of $40\,^{\circ}C$, while the cathodic feeding has a dew point of $T_{dp,c} = 70\,^{\circ}C$.

As shown in Fig. 7 (a), at the initial stage ($t = 0$ min), the current distribution reveals significantly high values near the inlet of the parallel flow channels, which is resulted from the incoming fresh oxygen. With increasing time, the local maximum current drops gradually; thus, the current distribution is leveled off. The phenomena may be explained as follows. When the oxygen of dew point $T_{dp,c} = 70\,^{\circ}C$ enters a cold environment (i.e., $T_{cell} = 40\,^{\circ}C$), the water vapor becomes supersaturated. Therefore, a large amount of water

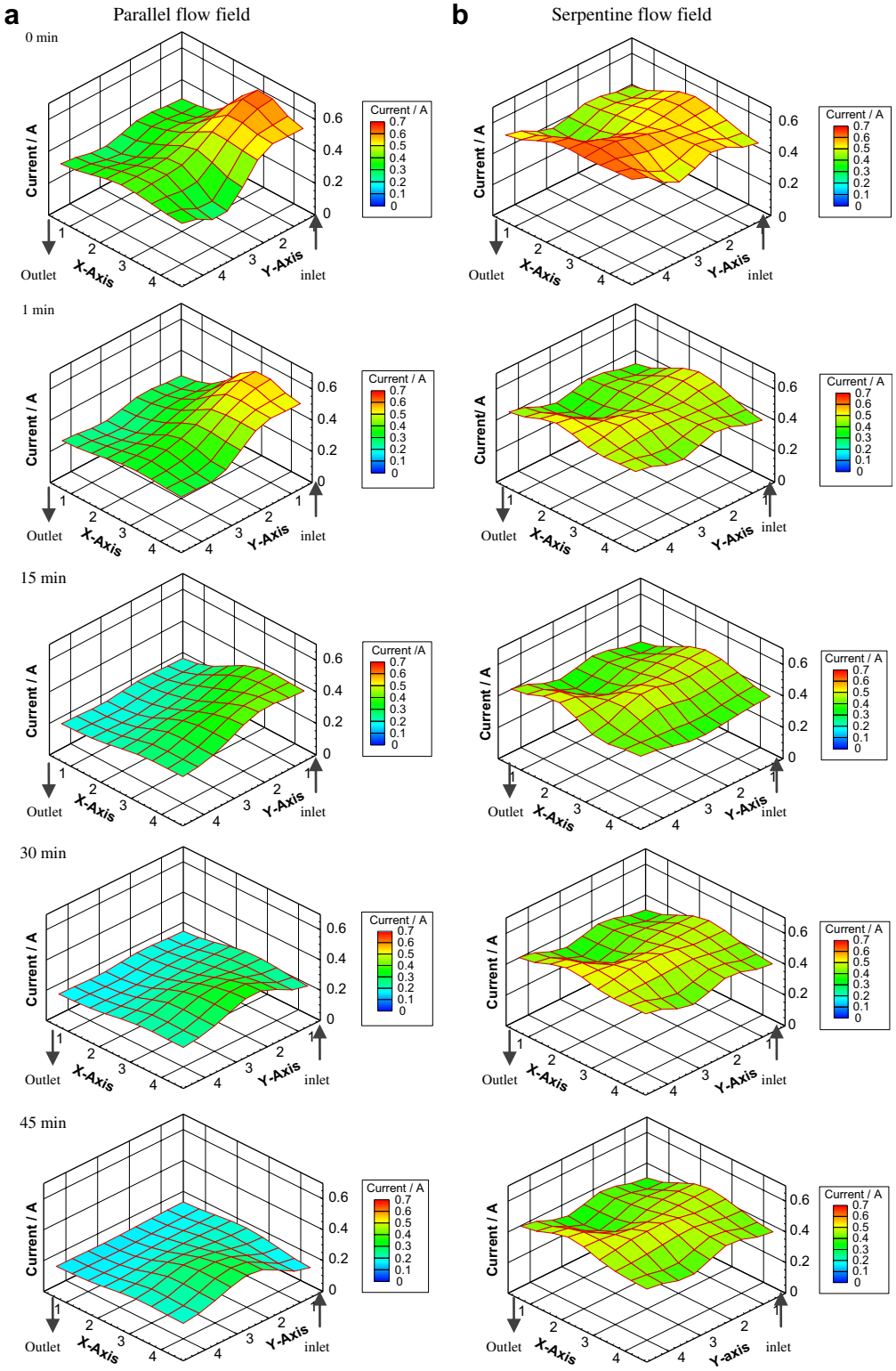

Fig. 7 – Transient developments of the local current distribution, (a) parallel flow field and (b) serpentine flow field, $U = 0.5$ V, $T_{cell} = 40$ °C, $\xi_a = 1.5$ and $\xi_c = 2.5$.

vapor is condensed to liquid form. In addition, the ORR generates some liquid water. All liquid water in the electrode should be removed to keep the electrochemical reaction. However, the pressure gradient for flow across the parallel channels is too small to drive out the liquid water. The liquid water blocks the flow and thus retards the electrochemical reaction. In contrast, as shown in Fig. 7 (b), the current distribution on the serpentine flow-field plate is relatively uniform at the initial stage. Then it decreases slightly and soon reaches to a steady distribution. The slight decline in

local current in the startup period (from 0 min to 1 min) is because of an increase in the oxygen usage. The quickly stabilized current distribution is due to the good water management in the serpentine flow field. In general, a significant pressure gradient in the serpentine flow channels can keep the water in good movement. Thus, the performance remains stable without water accumulation in the electrode even after a long-term test. Note that the steady-state distributions of local current shown in Fig. 7 (b) reveal a slight bumper near the middle of the reaction region where is the straight portions of the serpentine flow channels. That is, the local current around the 180° return regions is smaller than that on the straight counterparts. This is because the liquid water is trapped easily as the flow turns around the 180° returns [31], and thus reduces the electrochemical reaction. This is caused mainly by the longer residence times of the velocity distribution of the core gas flow. Particle image velocimetry (PIV) measurements [32] in the U-shaped channel identified the regions of recirculation and flow separation.

4.3. *Parametric studies*

Fig. 8 further shows a comparison of the effect of cathodic-feeding dew point ($T_{dp,c}$ = 40–70 °C) on the cell performance between the parallel flow field and the serpentine flow field. Both the dew point of the anodic feedings and the cell operational temperature are fixed at 40 °C. The anodic and cathodic flow rates are fixed at stoichiometry $\xi_a = 1.5$ and $\xi_c = 2.5$, respectively. The operational voltage of the cell is fixed at $U = 0.5$ V. It is seen from Fig. 8 that at the low dew point of the cathodic feedings, $T_{dp,c} = 40$ °C, the current delivered by the single cell with a parallel flow field is almost the same as that with a serpentine flow-field. As the cathodic-feeding dew point increases, the current for the parallel flow field decreases drastically, while, in contrast, the current in the serpentine flow-field changes slightly. As mentioned above, when the saturated reactants with a high dew point (e.g., 70 °C) enters a cold flow field ($T_{cell} = 40$ °C), a large amount of water vapor will be condensed. The excess of liquid water not only blocks the flow channels along with the gas diffusion layer that increases the concentration polarization, but also covers the reacting site in the catalyst layer. Both effects will reduce the electrochemical reaction rate in a PEM fuel cell. As shown in Fig. 8, in the parallel flow channels, an increase in cathodic-feeding dew point from $T_{dp,c} = 40$ °C to 70 °C results in a decrease in current from 8.2 to 5.5 A, with a reduction of the electrochemical performance about 30%. Using the serpentine flow channels instead of the parallel ones, the current reduction is only 5%. This is because the serpentine flow channels have high-pressure drops along the flow direction that can drive the liquid water downstream. Contrarily, the pressure drops across the parallel flow channels cannot well remove the water from the porous cathode. Thus, it can be concluded that the serpentine flow channels perform better than the parallel flow channels due to their superior in water management.

Fig. 9 shows the local current distributions on the biomimic flow-field plate under three different cell voltages, i.e., 0.3, 0.5 and 0.7 V. The cell operational temperature and the dew point for both feedings are fixed at 60 °C. The stoichiometries of hydrogen and oxygen are maintained at $\xi_a = 1.5$ and $\xi_c = 2.5$, respectively. It is seen from the figure that the current distribution is raised by the decrease in cell operational voltage. At the high cell voltage of 0.7 V, the local current distribution is rather uniform. However, at low operational voltage of 0.3 V, the distributions of the local current on the cathodic flow-field plate are relatively uneven.

Fig. 10 shows the effect of stoichiometry of the cathodic feedings on the local current distributions on the biomimic flow-field plate. The cell operational temperature and voltage are fixed at $T_{cell} = 60$ °C and $U = 0.6$ V, respectively. The dew point for both feedings is fixed at 60 °C while the hydrogen stoichiometry is kept at $\xi_a = 1.5$. It is seen from this figure that the effect of oxygen flow rate on the local current distribution is negligible as the cathodic stoichiometry is varied from $\xi_c = 2.5$ to $\xi_c = 3.5$.

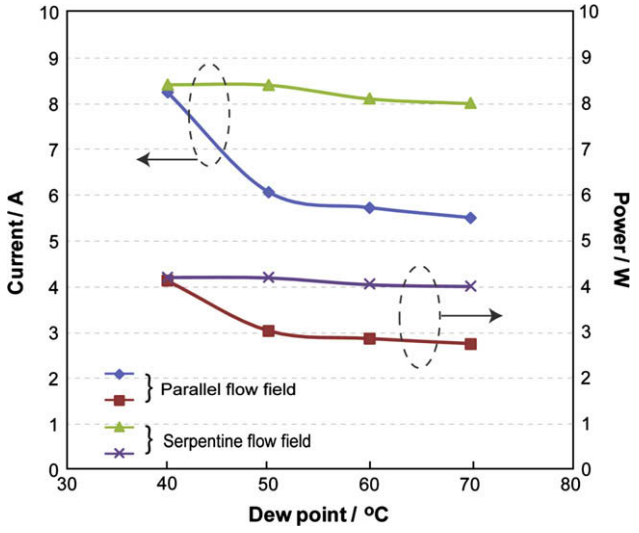

Fig. 8 – Effect of dew point of cathodic feedings on the current and power for parallel and serpentine flow fields, $U = 0.5$ V, $T_{cell} = 40$ °C, $\xi_a = 1.5$ and $\xi_c = 2.5$.

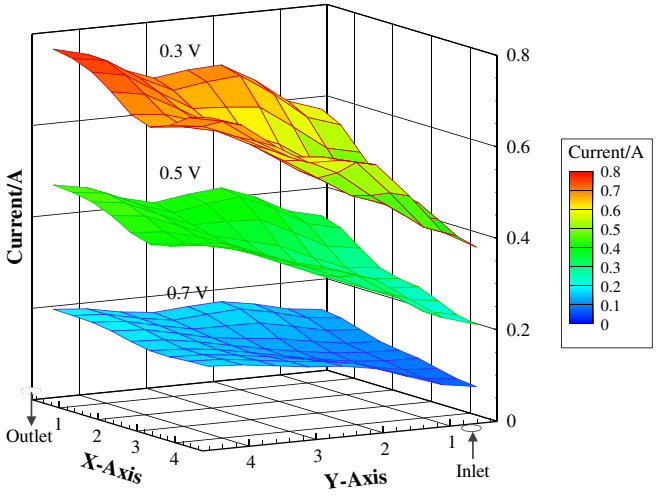

Fig. 9 – Local current distributions under different operating voltages, biomimic flow-field plate, $T_{cell} = 40$ °C, $\xi_a = 1.5$ and $\xi_c = 2.5$.

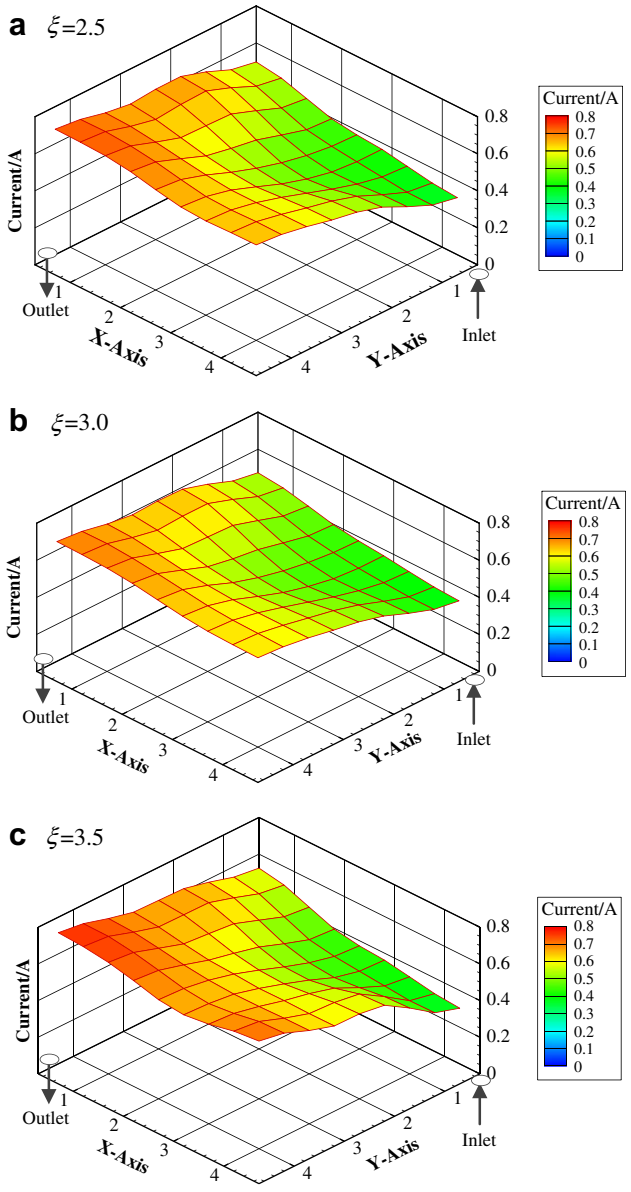

Fig. 10 – Effect of stoichiometry of cathodic feedings (oxygen flow rate) on the local current distribution on biomimic flow field, (a) $\xi = 2.5$, (b) $\xi = 3.0$ and (c) $\xi = 3.5$, $U = 0.6$ V, $T_{cell} = 60$ °C.

Fig. 11 shows a comparison of the polarization curves among the three different flow fields, i.e., interdigitated, serpentine and biomimic flow fields. Both the dew point of the cathodic feedings and the cell operational temperature are 60 °C. The anodic and cathodic feedings have flow rates of $\xi_a = 1.5$ and $\xi_c = 2.5$, respectively. It is clearly seen that the serpentine flow field performs best among the three flow fields as the cell operational voltage is less than 0.8 V. At high operational voltage ($U > 0.8$ V), the performance of the biomimic flow field is slightly better than the serpentine flow field. Noteworthy from the above discussion that using the same MEA under the same operational conditions, switching the flow-field plate means altering the mass transfer mechanisms in the fuel cell. That is, the local current distribution is affected

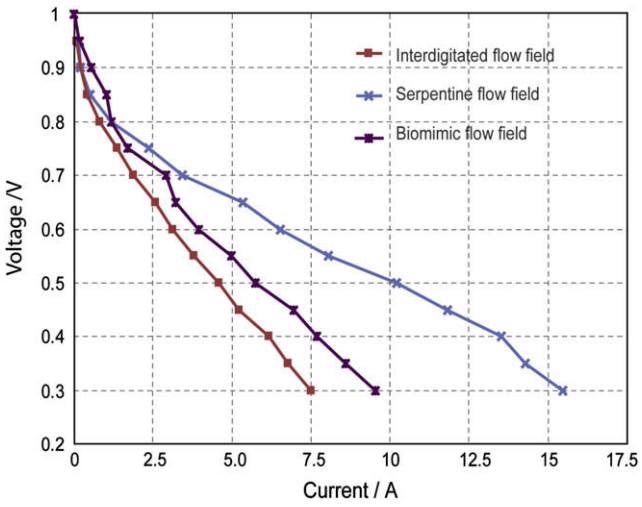

Fig. 11 – Comparison of performance among three different flow fields, $T_{cell} = T_{dp,c} = 60$ °C, $\xi_a = 1.5$ and $\xi_c = 2.5$.

by the flow-field patterns via altering the convection/diffusion mechanisms. The present results have demonstrated that the serpentine flow field is more favorable than other types of flow fields due to its stronger mass transfer ability.

5. Conclusions

This paper has demonstrated a new technique for determination of regionally averaged current distributions in a PEM fuel cell. The technique is mapping the current distribution on a special-designed composited plate with an array of segmented current collectors. A 16-channel multiplexer with an array of Hall-effect current sensors simultaneously detects transient distribution of the local currents on the composite plate. A self-made membrane electrode assembly is sandwiched between the cathodic composite plate and an anodic stainless-steel plate. The effects of the cathodic flow-field patterns (parallel, serpentine, interdigitated and biomimic flow fields), the cathodic-feeding stoichiometries ($\xi_c = 2.5$–3.5) and the dew point of cathodic feedings ($T_{dp,c} = 40$–70 °C) on the current distribution on a PEM fuel cell have been examined. Results showed that the local current distributions obtained by the present composite plate are compared well with the numerical results. The higher the operational voltage is, the more uniform the local current distribution become. The evolution of local current distribution further showed that the serpentine flow field performs best among the flow fields investigated due to its superior in mass transfer capability as well as in water management. Moreover, from the local current distribution in the serpentine flow field, it is found that the liquid water entraps easily in the corners of the 180° return that reduces the electrochemical reaction.

Acknowledgements

This work was partly sponsored by the National Science Council of Taiwan under contract No. NSC 95-2212-E-216-003.

REFERENCES

[1] Hwang JJ, Wang DY, Shih NC. Development of a lightweight fuel cell vehicle. J Power Sources 2005;141:108–15.
[2] Noponen M, Mennola T, Mikkola M, Hottinen T, Lund P. Measurement of current distribution in a free-breathing PEMFC. J Power Sources 2002;106:304–12.
[3] Ghosh PC, Wüster T, Dohle H, Kimiaie N, Mergel J, Stolten D. In situ approach for current distribution measurement in fuel cells. J Power Sources 2006;154:184–91.
[4] Dutta S, Shimpalee S, Van Zee JW. Numerical prediction of mass-exchange between cathode and anode channels in a PEM fuel cell. Int J Heat Mass Transfer 2001;44: 2029–42.
[5] Stumper J, Campbell SA, Wilkinson DP, Johnson MC, Davis M. In-situ methods for the determination of current distributions in PEM fuel cells. Electrochim Acta 1998;43: 3773–83.
[6] Cleghorn SJC, Derouin CR, Wilson MS, Gottesfeld S. A printed circuit board approach to measuring current distribution in a fuel cell. J Appl Electrochem 1998;28:663.
[7] Yoon YG, Lee WY, Yang TH, Park GG, Kim CS. Current distribution in a single cell of PEMFC. J Power Sources 2003; 118:193–9.
[8] Sun H, Liu H, Guo LJ. PEM fuel cell performance and its two-phase mass transport. J Power Sources 2005;143:125.
[9] Hakenjos A, Hebling C. Spatially resolved measurement of PEM fuel cells. J Power Sources 2005;145:307–11.
[10] Ghosh PC, Wuster T, Dohle H, Kimiaie N, Mergel J, Stolten D. In situ approach for current distribution measurement in fuel cells. J Power Sources 2006;154:184–91.
[11] Eckl R, Grinzinger R, Lehnert W. Current distribution mapping in polymer electrolyte fuel cells – a finite element analysis of measurement uncertainty imposed by lateral currents. J Power Sources 2006;154:171–9.
[12] Strickland G, Litster S, Santiago JG. Current distribution in polymer electrolyte membrane fuel cell with active water management. J. Power Sources 2007;174:272–81.
[13] Wahdame, Candusso D, Francois X, Harel F, Pera M, Hissela D, et al. Comparison between two PEM fuel cell durability tests performed at constant current and under solicitations linked to transport mission profile. Int J Hydrogen Energy 2007;32:4523–36.
[14] Scott Weil K, Xia G, Yang ZG, Kim JY. Development of a niobium clad PEM fuel cell bipolar plate material. Int J Hydrogen Energy 2007;32:3724–33.
[15] Sun H, Zhang G, Guo L, Dehua S, Liu H. Effects of humidification temperatures on local current characteristics in a PEM fuel cell. J Power Sources 2007;168:400–7.
[16] Sauer DU, Sanders T, Fricke B, Lofer TB, Wippermann K, Kulikovsky AA, et al. Measurement of the current distribution in a direct methanol fuel cell – confirmation of parallel galvanic and electrolytic operation within one cell. J Power Sources 2008;176:477–83.
[17] Wang L, Liu H. Separate measurement of current density under the channel and the shoulder in PEM fuel cells. J Power Sources 2008;180:365–72.
[18] Sun H, Zhang G, Guo LJ, Liu H. A novel technique for measuring current distributions in PEM fuel cells. J Power Sources 2006;158:326–32.
[19] Hartnig C, Manke I, Kardjilov N, Hilger A, Grunerbel M, Kaczerowski J, et al. Combined neutron radiography and locally resolved current density measurements of operating PEM fuel cells. J Power Sources 2008;176:452–9.
[20] Hwang JJ, Liu CC, Savinell RF, Wainright J. A three-dimensional numerical simulation of the transport phenomena in the cathodic side of a PEMFC. J Appl Electrochem 2004;34:217.
[21] Hwang JJ, Chen PY. Heat/mass transfer in porous electrodes of fuel cells. Int J Heat Mass Transfer 2006;49: 2315–27.
[22] Wang Y, Wang CY. A nonisothermal, two-phase model for polymer electrolyte fuel cells. J Electrochem Soc 2006;153: A1193–200.
[23] Pasaogullari U, Wang CY. Liquid water transport in gas diffusion layer of polymer electrolyte fuel cells. J Electrochem Soc 2004;151:A399–406.
[24] Jung HM, Lee WY, Park JS, Kim CS. Numerical analysis of a polymer electrolyte fuel cell. Int J Hydrogen Energy 2004;29: 945–54.
[25] Hwang JJ. A complete two-phase model of a porous cathode of a PEM fuel cell. J Power Sources 2007;164:174–81.
[26] Hwang JJ, Chao CH, WU W. Thermal-fluid transports in a five-layer membrane-electrode assembly of a PEM fuel cell. J Power Sources 2006;163:450–9.
[27] Eckl R, Grinzinger R, Lehnert W. Current distribution mapping in polymer electrolyte fuel cells – a finite element analysis of measurement uncertainty imposed by lateral currents. J Power Sources 2006;154:171–9.
[28] Shimpalee S, van Zee JW. Numerical studies on rib & channel dimension of flow-field on PEMFC performance. Int J Hydrogen Energy 2007;32:842–56.
[29] Hwang JJ. Thermal-electrochemical modeling of a PEM fuel cell. J Electrochem Soc 2006;153:A216–24.
[30] Hwang JJ, Chao CH. Modeling of two-phase temperatures in a two-layer porous cathode of polymer electrolyte fuel cells. Int J Hydrogen Energy 2007;32:405–14.
[31] Martin J, Oshkai P, Djilali N. Flow structures in a U-shaped fuel cell flow channel: quantitative visualization using particle image velocimetry. ASME J Fuel Cell Sci Technol 2005;2:70–80.
[32] Spernjak D, Prasad AK, Advani SG. Experimental investigation of liquid water formation and transport in a transparent single-serpentine PEM fuel cell. J Power Sources 2007;170:334–44.